

**Structure II gas hydrates found below the bottom-simulating reflector**

M. Paganoni<sup>1</sup>, J. A. Cartwright<sup>1</sup>, M. Foschi<sup>1</sup>, R. C. Shipp<sup>2</sup>, and P. Van Rensbergen<sup>3</sup>

<sup>1</sup>Department of Earth Sciences, University of Oxford, South Parks Road, Oxford OX1 3AN, UK.

<sup>2</sup>Shell Exploration and Production Inc., Houston, TX, United States.

<sup>3</sup>Shell International Global Solutions B.V., Rijswijk, Netherlands.

Corresponding author: Matteo Paganoni (matteop@earth.ox.ac.uk)

**Contents of this file**

Additional information

Methods to estimate gas hydrate saturation

Gas geochemistry

Figures S1 to S7

Tables S1 to S6

References

**Introduction**

This supporting information file contains additional text, 7 figures and 6 tables. Figures include: (1) The porosity estimated from density logs at DC\_E and DC\_F; (2) Two seismic sections passing through the study area, showing (A) the cross-cutting relationship between the BSR and stratigraphic reflectors and (B) the reduction in frequency associated with the attenuated zone below the BSR; (3) An example of the MSCL-S measurements (P-wave velocity and gamma density) on a pressure core (FPC#8), retrieved approximately at the BSR depth; (4) A static resistivity image passing through the GHSZ at DC\_E; (5) The phase resistivity vs depth profile at DC\_F; (6) The horizontal and vertical resistivity vs depth profile at DC\_F and (7) The plot of excess pore pressure vs depth at DC\_E. Tables include: (1) All the chlorinity measurements undertaken at DC\_E; (2) A list of the parameters used to calculate hydrate saturation from chlorinity at DC\_E; (3) The average gas hydrate saturation ( $Sh$ ; % of pore space) for each core at DC\_E, estimated from chlorinity measurements; (4) The average  $Sh$  for each core at DC\_E, estimated from pressure core depressurization experiments; (5) The average core gas composition from gas chromatography analyses at DC\_E and (6) The temperatures measured at DC\_E used to estimate the geothermal gradient. Depths are expressed both in meters below the seafloor (mbsf) and below the sea level (mbsl).

### **Additional information. Methods to estimate gas hydrate saturation**

We calculated gas hydrate saturation ( $Sh$ , % of pore space) from chlorinity by the difference between the measured ( $Cm$ ) and the baseline ( $Cb$ ) chlorinity [Malinverno *et al.*, 2008] (Table S1 in the supporting information).  $Sh$  equals to:

$$Sh = 100(\beta(Cb - Cm)/(Cm + \beta(Cm - Cb)))$$

Where  $\beta$  is a dimensionless coefficient accounting for the density change from gas hydrate to water and equals to:

$$\beta = (\rho_w N V)/(n_w m_w)$$

Where  $\rho_w$  is the water density (g/cc),  $N$  is the Avogadro's number,  $V$  is the volume of the hydrate elementary cell,  $n_w$  is the number of water molecules in the hydrate elementary cell and  $m_w$  is the molar mass of water (Table S2 in the supporting information).

We estimated  $Sh$  from pressure core depressurization assuming a 100% methane composition and knowing the methane solubility in water at in situ conditions, from the excess moles of gas [Kim *et al.*, 2013; Lee *et al.*, 2013; Holland and Schultheiss, 2014]. The errors introduced by the presence of a gas mixture instead of a pure methane phase were probably small, since the  $Sh$  values obtained in FPC cores from chlorinity and depressurization data produced similar results (Tables S3 and S4 in the supporting information).

Finally, the phase shift deep smoothed resistivity (which is the measurement that better penetrates into the formation) and porosity data from density logs were used to estimate  $Sh$  in the four wells, taking due account of hydrate-related fractures and associated anisotropy in the sediment. Due to the lack of density logs for wells L\_2 and M\_1, we interpolated the porosity values obtained at DC\_E and DC\_F (Figure S1 in the supporting information) to obtain a porosity VS depth profile for these locations. We then followed the methodology proposed by Lee and Collett [2012] and used a ‘‘fracture porosity’’ ranging from 3.5% to 5.0%, (i.e. 95.0-97.5% of the fracture space is filled by hydrates) and a fracture dip angle of 70°, based on observations on resistivity images. These values are convenient parameters and are used to provide reliable estimates of  $Sh$ , if calibrated with direct measurements. The calculations resulted in two  $Sh$  profiles for each wells, using resistivity data, corresponding to a lower and an upper end-member.

### **Additional information. Gas geochemistry**

Analyses on core samples sent to Core Labs revealed small fractions of C<sub>5</sub>-C<sub>9</sub> hydrocarbons, suggesting the presence of minor amounts of structure H hydrates [Sassen and MacDonald, 1994; Lu *et al.*, 2007]. Unfortunately, no quantitative information about these analyses has been provided to us. However, this corroborates the hypothesis of a direct link between the hydrate system and the underlying thermogenic reservoir, which contains on average 1.24% of C<sub>5+</sub> hydrocarbons in its gas zone.

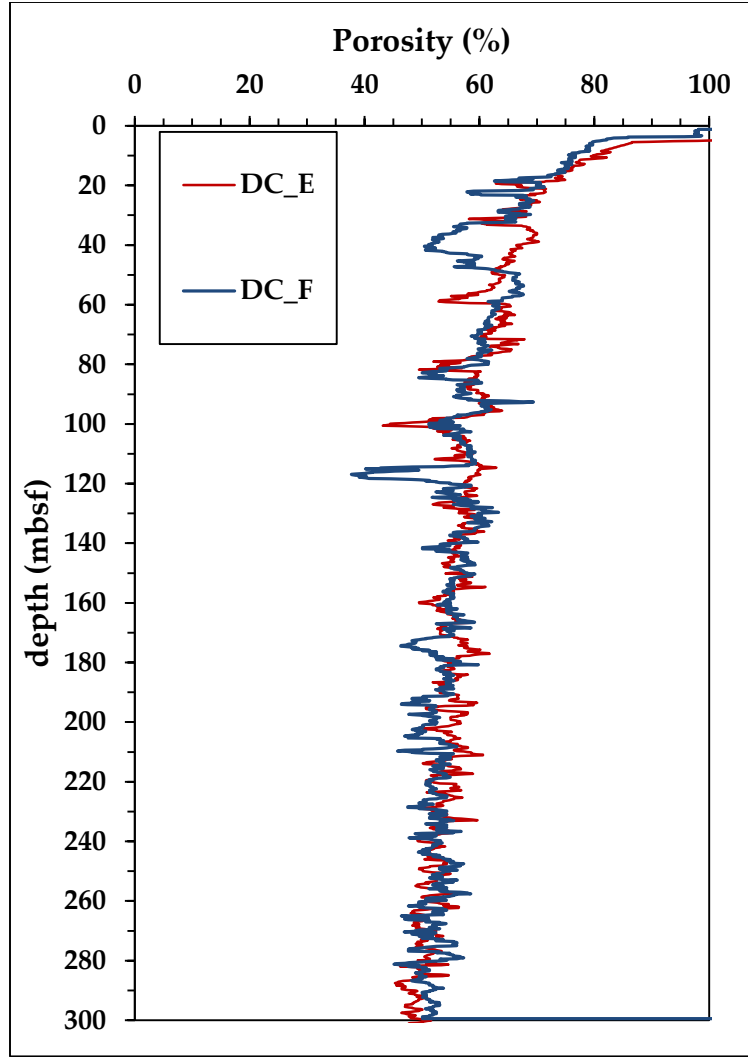


**Figure S1.** Porosity profiles at DC\_E and DC\_F. The porosity has been calculated from density logs. The neutron logs are affected by clay minerals and provide overestimated values [Cook *et al.*, 2008]. Porosity values were used to estimate hydrate saturation, in terms of % of pore space. For the wells M\_1 and L\_2, we obtained a porosity VS depth profile interpolating porosities at DC\_E and DC\_F, given the little changes, in terms of stratigraphy, between these four wells.

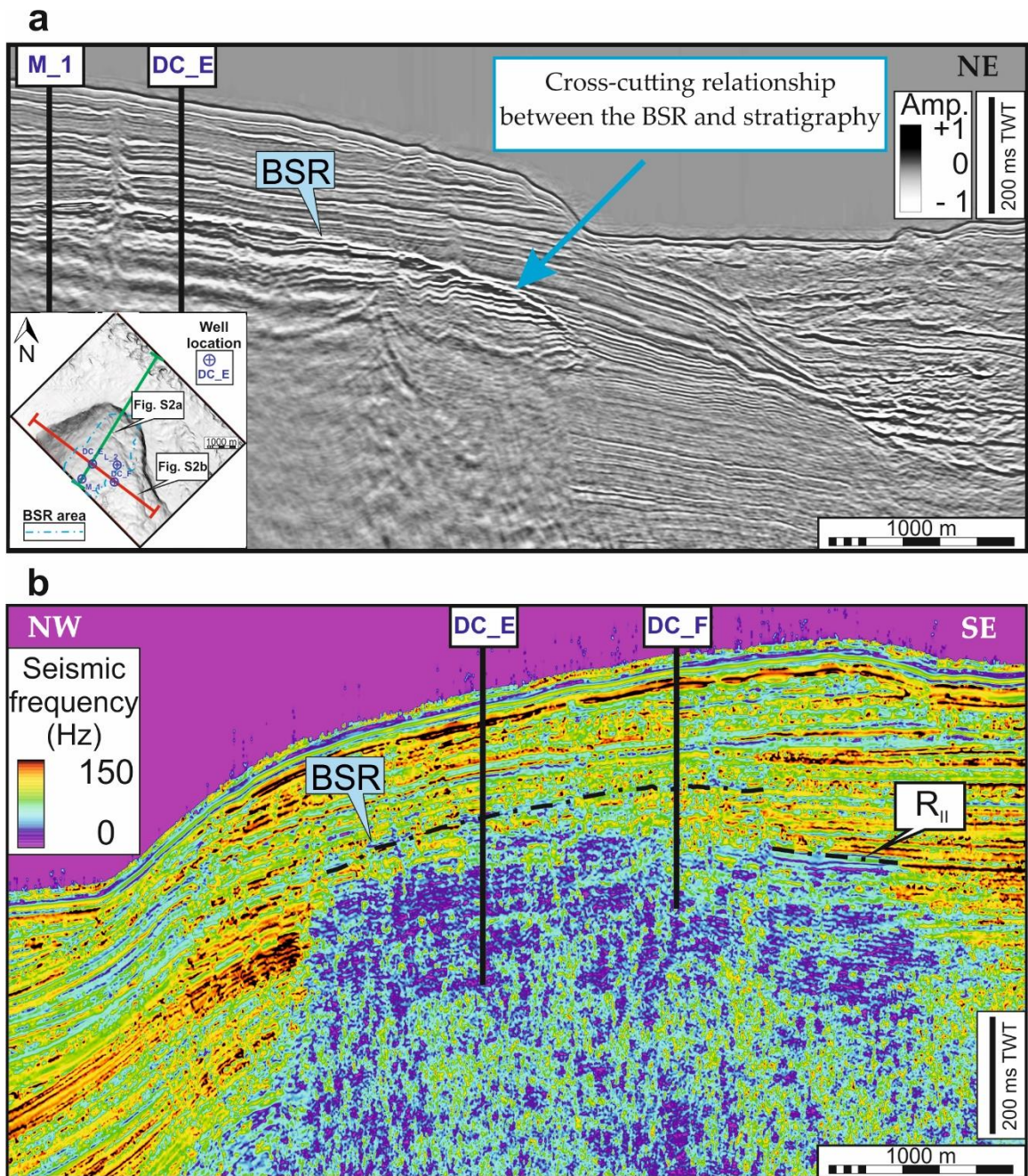


**Figure S2.** (a) Seismic section showing the BSR at the top of the anticline and its cross-cutting relationship with stratigraphy. (b) Instantaneous frequency section along the same path of figure 1b, displaying the strong frequency reduction below the BSR and below R<sub>II</sub>, suggesting the presence of free gas. The locations of the seismic sections (green and red arrows) are indicated in the inset seafloor map.

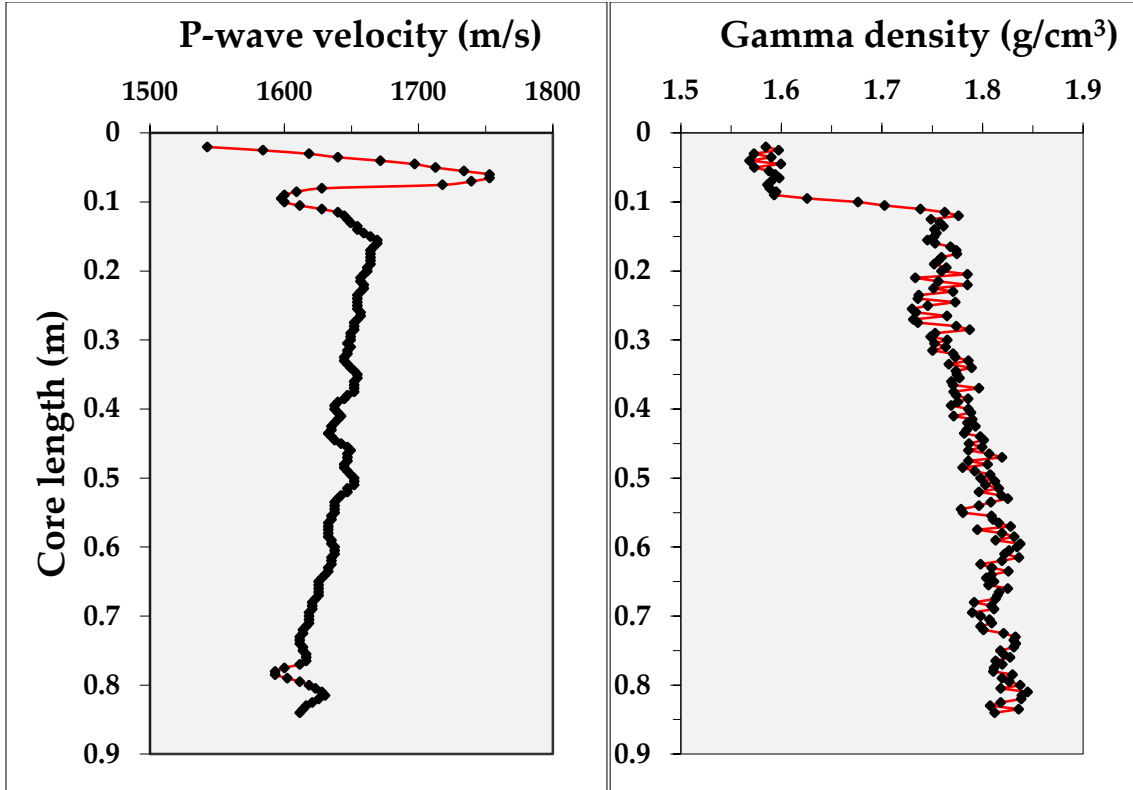


**Figure S3.** Example of P-wave velocity (left) and gamma density (right) measurements on a pressure core (FPC#8, Figure 3a), approximately located at the BSR depth. No free gas was detected, since the velocity profile is relatively linear, except for the upper part of the core, where relatively high values have been observed. These high velocities correspond to a bright zone observed in the X-ray image (see Figure 3a) and are related to gas hydrates, probably at moderate to high saturation. The presence of gas hydrates in the upper portion of the core is also confirmed by the relatively low gamma density values compared to the rest of the core [Riedel *et al.*, 2010].

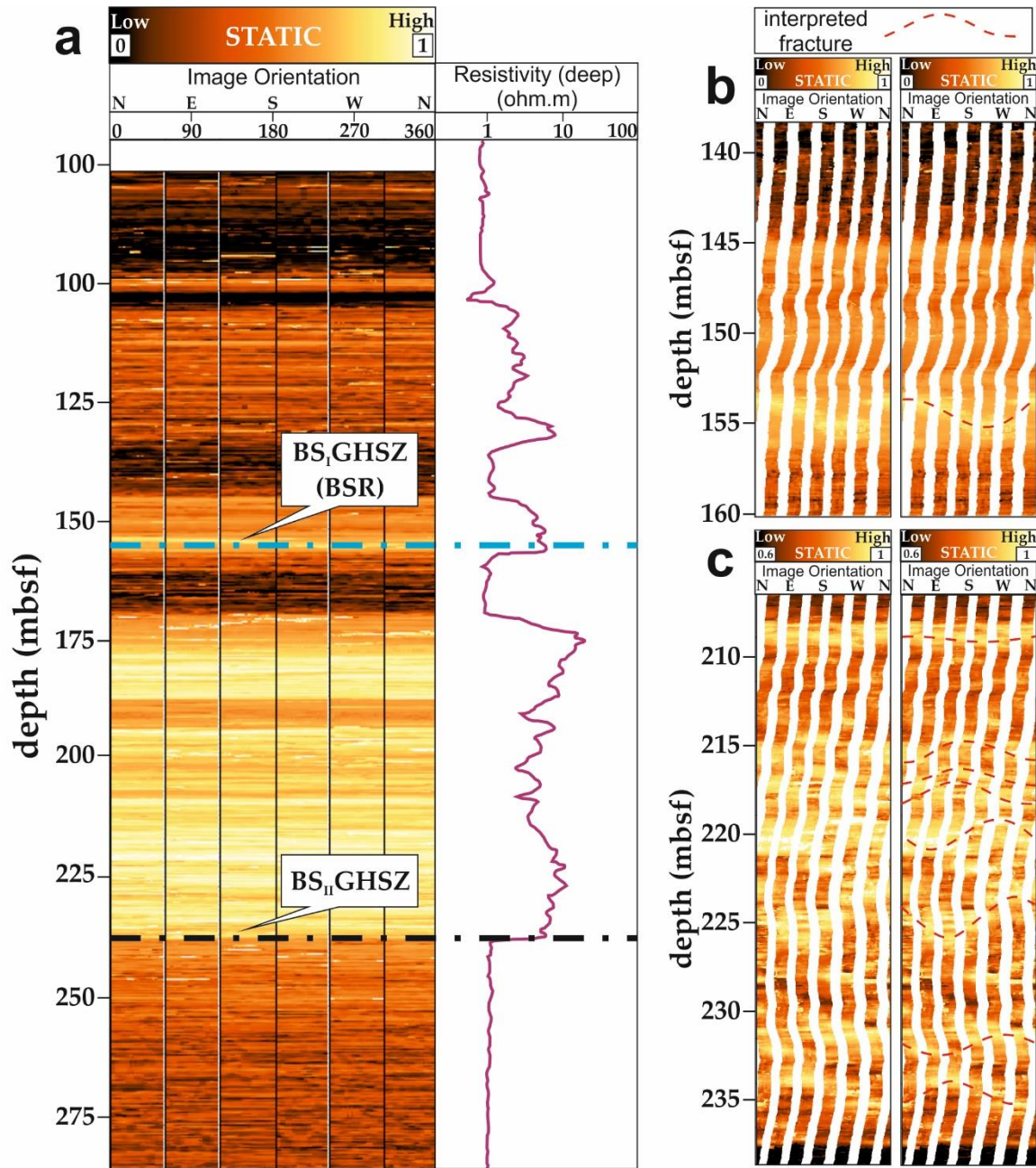


**Figure S4.** Resistivity images (static) at DC\_E. (a) General view. Bright colors are related to resistive material, in this case interpreted to be hydrate bearing sediments, possibly including traces of free gas below the BS<sub>I</sub>GHSZ (i.e. the BSR) [Riedel et al., 2010]. The position of the interpreted BS<sub>I</sub>GHSZ and BS<sub>II</sub>GHSZ are indicated with a blue and black dotted line, respectively. The seafloor is 948.54 m deep at DC\_E. (b) and (c) Detailed resistivity images showing sinusoidal features, interpreted to represent fracture-filling hydrates approximately at the BS<sub>I</sub>GHSZ (~153 mbsf, b) and above the BS<sub>II</sub>GHSZ (~237 mbsf, c)

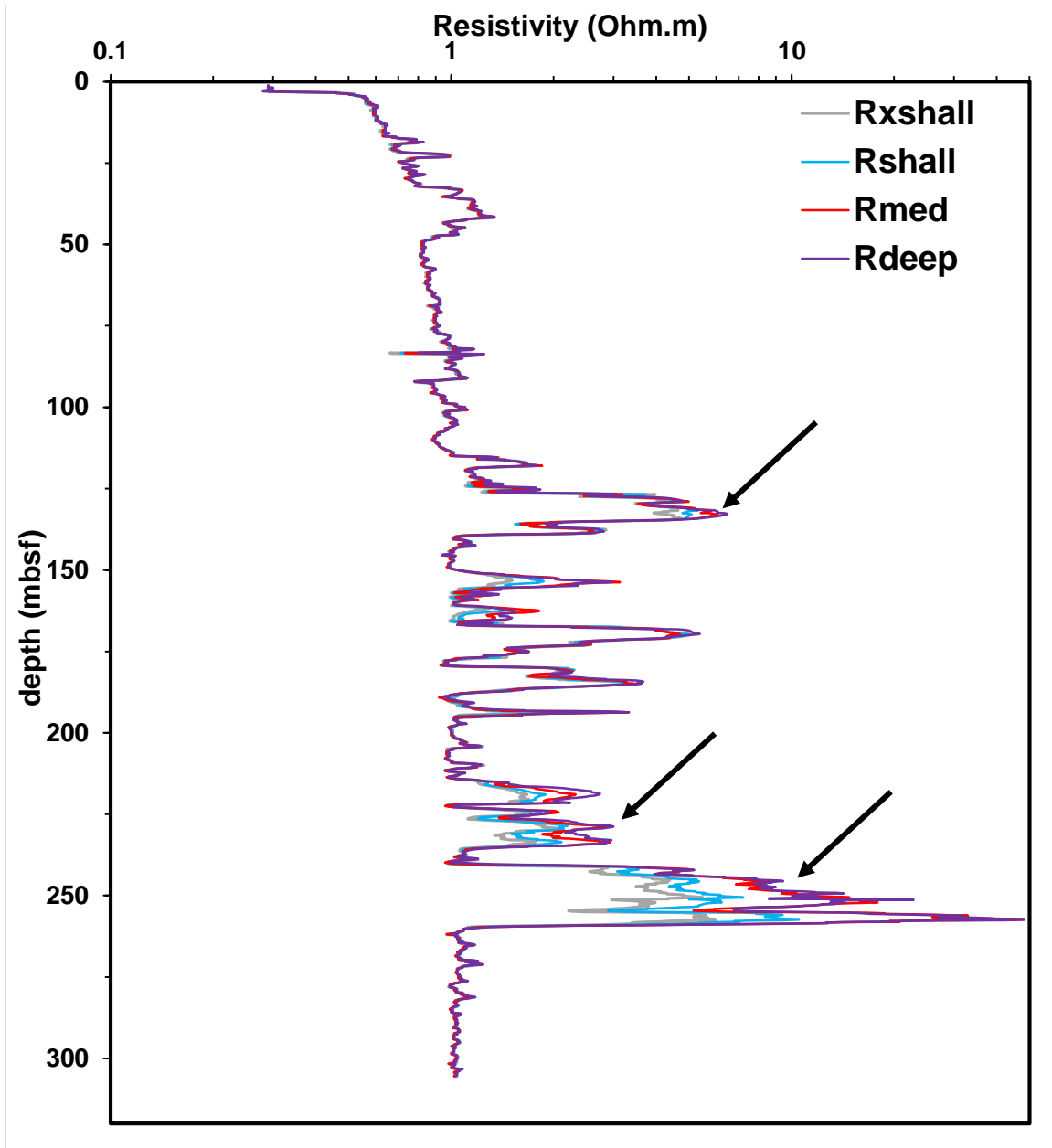


**Figure S5.** Resistivity VS depth profile (DC\_F) showing separation (black arrows) between extra-shallow (Rxshall.), shallow (Rshall), medium (Rmed) and deep (Rdeep) phase resistivity, acquired with the EWR®-Phase 4 multiarray propagation tool.

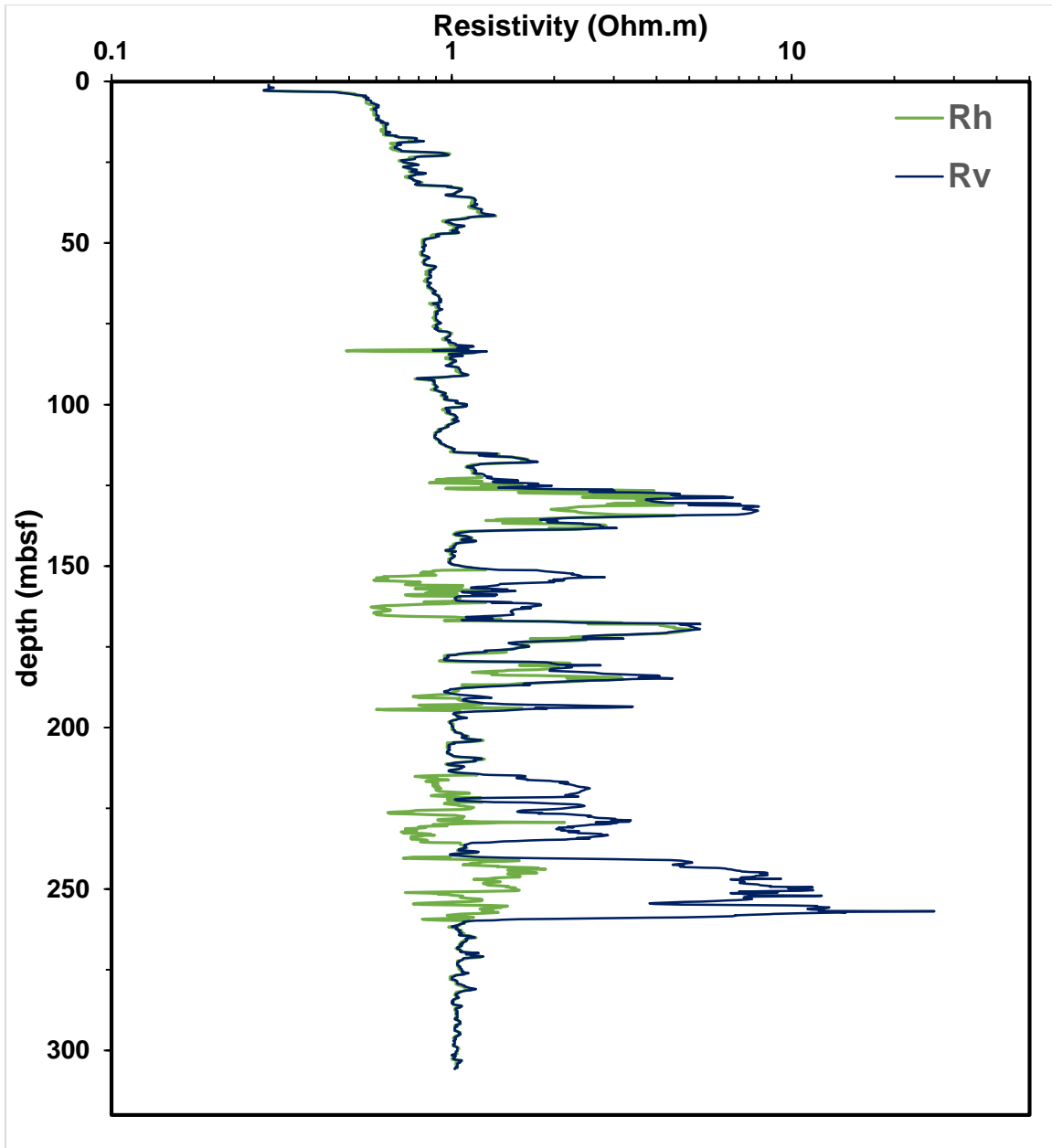


**Figure S6.** Horizontal (Rh) and vertical (Rv) Resistivity VS depth profile (DC\_F), acquired with the EWR®-Phase 4 multiarray propagation tool. The marked difference between Rh and Rv (black arrows), with Rv higher than Rh, suggests the presence of resistive sub-vertical features, interpreted to be filled with gas hydrates [Cook *et al.*, 2010].

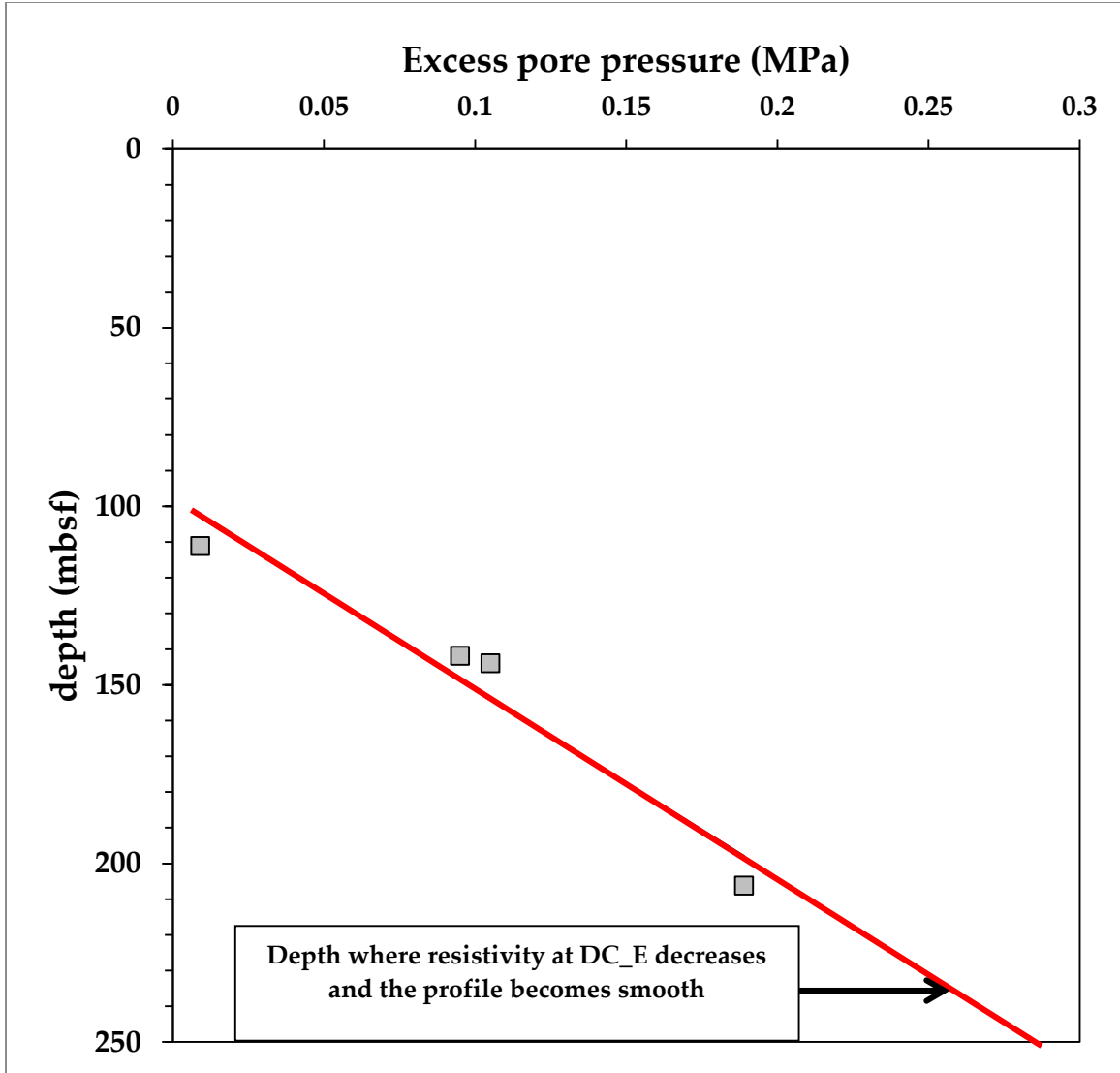


**Figure S7.** Excess pore pressure profile at DC\_E. Pressure was measured using a wireline-operated piezoprobe equipped with two pressure sensors. Four tests were accomplished at DC\_E. For each test the piezoprobe was pushed into the soil beyond the bottom of the borehole and pore pressure with time was recorded. We extrapolated a linear increase of excess pore pressure with depth ( $R^2 = 0.94$ ). The total pore pressure at a certain depth, which has been used to calculate the hydrate stability, is the sum of the hydrostatic and the excess pore pressure.

**Table S1.** Chloride concentration data for DC\_E. To see these data, look at the separate Excel file. Shelby= Shelby tube data; FPC#= Fugro Pressure Corer data; FC#= Fugro Corer data;  $C_m$  (corrected) = measured Chloride concentration (chlorinity), corrected for drill water infiltration;  $C_b$ = baseline chlorinity. There is no evidence of hydrates for the first 60 mbsf, where  $C_b$  is supposed to be equal to  $C_m$ .

Parameter	
$V$ (structure I)	$1.728 \times 10^{21} \text{ cm}^3$
$nw$ (structure I)	46
$\beta$ (structure I)	1.257
$V$ (structure II)	$5.178 \times 10^{21} \text{ cm}^3$
$nw$ (structure II)	136
$\beta$ (structure II)	1.274

**Table S2.** Parameters used to calculate hydrate saturation from chlorinity. The values have been taken from *Malinverno et al.* [2008] and *Carrol* [2014].

Core	Average depth (mbsf)	Average depth (mbsl)	Average <i>Sh</i> (% pore space)
Shelby17	60.4	1008.9	1.89
FPC#1	89.1	1037.7	0.32
FPC#2	89.5	1038.1	0.48
Shelby19	90.2	1038.8	0.00
FC#1	105.5	1054.1	1.82
FPC#13	114.9	1063.4	3.57
Shelby21	120.5	1069.0	2.68
FPC#3	126.3	1074.9	3.68
FC#2	127.0	1075.5	3.83
FPC#4	127.5	1076.0	1.88
FPC#5	137.0	1085.5	2.18
FPC#6	143.4	1092.0	2.92
Shelby23	150.5	1099.0	11.11
FPC#7	151.8	1100.3	3.20
FPC#8	152.9	1101.4	7.44
FC#3	154.8	1103.3	2.58
FPC#9	161.4	1109.9	3.98
FPC#10	171.4	1119.9	9.21
FC#5	180.8	1129.3	7.48
Shelby25	184.0	1132.6	3.17
FC#6	192.5	1141.1	18.17
FC#7	197.1	1145.7	11.11
FC#9	208.0	1156.6	9.40
Shelby27	210.1	1158.7	0.00
FC#10	212.6	1161.2	9.72
FC#11	217.2	1165.8	5.32
FC#12	219.3	1167.8	11.77
FPC#11	221.4	1169.9	11.29
FC#13	231.3	1179.8	7.54
FC#14	233.0	1181.5	6.37
FC#15	239.4	1187.9	5.40
Shelby29	243.1	1191.7	4.07
FPC#12	249.1	1197.7	6.77
FC#16	277.9	1226.4	3.58
Shelby31	279.8	1228.3	0.04

**Table S3.** Average gas hydrate saturations (*Sh*) from pore-water freshening anomalies measured in conventional and pressure cores at DC\_E. Shelby= Shelby tube data; FPC#= Fugro Pressure Corer data; FC#= Fugro Corer data.

Pressure Core	Average depth (mbsf)	Average depth (mbsl)	Average $Sh$ (% pore space)
HRC#1	87.5	1036.0	0.00
FPC#1*	89.1	1037.7	–
FPC#2	89.5	1038.1	0.00
HRC#2	114.5	1063.0	–
FPC#13	114.9	1063.4	0.00
FPC#3*	126.3	1074.9	–
FPC#4*	127.5	1076.0	–
HRC#3	128.0	1076.5	–
HRC#4	135.5	1084.0	–
FPC#5*	137.0	1085.5	–
HRC#5	137.5	1086.0	0.00
FPC#6	143.4	1092.0	0.00
HRC#6	150.5	1099.0	2.64
FPC#7*	151.8	1100.3	–
FPC#8	152.9	1101.4	7.86
HRC#7	160.0	1108.5	8.94
FPC#9	161.4	1109.9	1.13
FPC#10	171.4	1119.9	7.49
FPC#11	221.4	1169.9	11.95
FPC#12	249.1	1197.7	8.50

**Table S4.** Average gas hydrate saturations ( $Sh$ ) from excess gas during depressurization experiments on pressure cores at DC\_E. HRC#= Hyace Rotary Corer data (core successful); FPC#= Fugro Pressure Corer data (core successful); **FPC#\***= Fugro Pressure Corer data (core unsuccessful, i.e. not retrieved under hydrate stability conditions).

Core	depth (mbsf)	depth (mbsl)	C <sub>1</sub> %	C <sub>2</sub> %	C <sub>3</sub> %	C <sub>4</sub> %
HRC#1	87.5	1036.0	99.9	0.1	–	–
FPC#2	89.5	1038.1	100	0	–	–
FPC#13	114.9	1063.4	98.84	0.93	0.23	–
HRC#5	137.5	1086.0	97.94	1.94	0.01	0.11
FPC#6	143.4	1092.0	97.47	2.28	0.04	0.21
HRC#6	150.5	1099.0	89.46	9.49	0.24	0.81
FPC#8	152.9	1101.4	92.29	7.17	0.12	0.42
FC#3	154.8	1103.3	91.59	8.41	–	–
HRC#7	160.0	1108.5	92.26	7	0.18	0.56
FPC#9	161.4	1109.9	95.69	4.22	0.03	0.06
FPC#10	171.4	1119.9	85.48	12.66	1.12	0.74
FC#5	180.8	1129.3	86.5	13.5	–	–
FC#6	192.5	1141.1	83.91	16.09	–	–
FC#9	208.0	1156.6	87.52	12.48	–	–
FC#11	217.2	1165.8	88.23	11.77	–	–
FC#12	219.3	1167.8	77.77	13.66	7.89	0.68
FPC#11	221.4	1169.9	90.26	7.36	2.09	0.29
FC#13	231.3	1179.8	88.17	11.83	–	–
FPC#12	249.1	1197.7	87.23	8.5	3.55	0.72
FC#16	277.9	1226.4	67.5	17.63	11.45	3.42

**Table S5.** Average core gas composition from gas chromatography analyses. HRC#= Hyace Rotary Corer data; FPC#= Fugro Pressure Corer data; FC#= Fugro Corer data; C<sub>1</sub>%= methane (%); C<sub>2</sub>%= ethane (%); C<sub>3</sub>%= propane (%); C<sub>4</sub>%= butane (%).

Test tool	depth (mbsf)	depth (mbsl)	T (°C)
CTD	0	948.54	4.58
PWS	32.5	981.04	6.76
Temperature Cone	43	1038.1	7.83
Temperature Cone	61	1063.4	8.58
Temperature Cone	93	1086	11.02
Temperature Cone	120	1092	12.62
Temperature Cone	150	1099	14.52
PWS	178	1101.4	16.1
PWS	179	1103.3	16.14
PWS	214	1108.5	18.05
Temperature Cone	234	1109.9	19.68

**Table S6.** Temperatures measured at DC\_E. The derived geothermal gradient is linear ( $R^2=0.99$ ) for the first 234 mbsf. Details about the test tools are explained in the Data and Methods section.

## References

- Carrol, J. J. (2014), *Natural Gas Hydrates. A Guide for Engineers* (Gulf Professional Publishers, ed. 3).
- Cook, A. E., D. S. Goldberg, and R. L. Kleinberg (2008), Fracture-controlled gas hydrate systems in the northern Gulf of Mexico, *Mar. Petrol. Geol.*, 25(9), 932-941, doi:10.1016/j.marpetgeo.2008.01.013.
- Cook, A. E., B. I. Anderson, A. Malinverno, S. Mrozewski, and D. S. Goldberg (2010), Electrical anisotropy due to gas hydrate-filled fractures, *Geophysics*, 75(6), F173-F185, doi: 10.1190/1.3506530.
- Holland, M., and P. Schultheiss (2014), Comparison of methane mass balance and X-ray computed tomographic methods for calculation of gas hydrate content of pressure cores, *Mar. Petrol. Geol.*, 58, 168-177, doi:10.1016/j.marpetgeo.2014.07.016.
- Kim, J. H., M. E. Torres, J. Y. Lee, W. L. Hong, M. Holland, M. H. Park, M. H., J. Choi, and G. Y. Kim (2013), Depressurization experiment of pressure cores from the central Ulleung Basin, East Sea: Insights into gas chemistry, *Org. Geochem.*, 62, 86-95, doi:10.1016/j.orggeochem.2013.07.010.
- Lee, M. W., and T. S. Collett (2012), Pore- and fracture-filling Gas hydrate reservoirs in the Gulf of Mexico Gas hydrate Joint Industry Project leg II Green Canyon 955 H well, *Mar. Petrol. Geol.*, 34(1), 62-71, doi:10.1016/j.marpetgeo.2011.08.002.
- Lee, J. Y., J. W. Jung, M. H. Lee, J.-J. Bahk, J. Choi, B.-J. Ryu, and P. Schultheiss (2013), Pressure core based study of gas hydrates in the Ulleung Basin and implication for geomechanical controls on gas hydrate occurrence, *Mar. Petrol. Geol.*, 47, 85-98, doi:10.1016/j.marpetgeo.2013.05.021.
- Lu, H., Y. Seo, J. Lee, I. Moudrakovski, J. A. Ripmeester, N. R. Chapman, R. B. Coffin, G. Gardner, and J. Pohlman (2007), Complex gas hydrate from the Cascadia margin, *Nature*, 445(7125), 303-306, doi:10.1038/nature05463.
- Malinverno, A., M. Kastner, M. E. Torres, and U. G. Wortmann (2008), Gas hydrate occurrence from pore water chlorinity and downhole logs in a transect across the northern Cascadia margin (Integrated Ocean Drilling Program Expedition 311), *J. Geophys. Res.*, 113, B08103, doi:10.1029/2008JB005702.
- Riedel, M., T. S. Collett, P. Kumar, A. V. Sathe, and A. Cook (2010), Seismic imaging of a fractured gas hydrate system in the Krishna–Godavari Basin offshore India, *Mar. Petrol. Geol.*, 27(7), 1476-1493, doi:10.1016/j.marpetgeo.2010.06.002.
- Sassen, R., and I. R. MacDonald (1994), Evidence of structure H hydrate, Gulf of Mexico continental slope, *Org. Geochem.*, 22(6), 1029-1032, doi:10.1016/0146-6380(94)90036-1.